



City Research Online

City, University of London Institutional Repository

Citation: Miao, X., Zhang, Q. ORCID: 0000-0003-0982-2986, Atkin, C.J. ORCID: 0000-0003-2529-1978, Sun, Z. and Li, Y. (2018). Improving Purge Air Cooling Effectiveness by Engineered End-Wall Surface Structures-Part II: Turbine Cascade. *Journal Of Turbomachinery*, 140(9), 091002. doi: 10.1115/1.4040854

This is the accepted version of the paper.

This version of the publication may differ from the final published version.

Permanent repository link: <http://openaccess.city.ac.uk/id/eprint/20897/>

Link to published version: <http://dx.doi.org/10.1115/1.4040854>

Copyright and reuse: City Research Online aims to make research outputs of City, University of London available to a wider audience. Copyright and Moral Rights remain with the author(s) and/or copyright holders. URLs from City Research Online may be freely distributed and linked to.

City Research Online:

<http://openaccess.city.ac.uk/>

publications@city.ac.uk

Improving Purge Air Cooling Effectiveness by Engineered End-Wall Surface Structures – Part II: Turbine Cascade

Xin Miao

e-mail: Xin.Miao@city.ac.uk

Qiang Zhang

e-mail: Qiang.Zhang.1@city.ac.uk

Chris Atkin

e-mail: Chris.Atkin.1@city.ac.uk

Zhengzhong Sun

e-mail: Zhengzhong.Sun@city.ac.uk

Department of Mechanical Engineering & Aeronautics
City, University of London
Northampton Square, London, EC1V 0HB, United Kingdom

Y S Li

e-mail: yansheng.li@siemens.com
Siemens Industrial Turbomachinery Limited
Lincoln LN5 7FD, UK

ABSTRACT

Motivated by the recent advances in Additive Manufacturing (AM), a novel turbine end-wall aerothermal management method is presented in this two-part paper. The feasibility of enhancing purge air cooling effectiveness through engineered surface structure was experimentally and numerically investigated. The fundamental working mechanism and improved cooling performance for a 90-degree turning duct are presented in Part I. The second part of this paper demonstrates this novel concept in a low-speed linear cascade environment. The performance in three purge air blowing ratios is presented and enhanced cooling effectiveness and net heat flux reduction were observed from experimental data, especially for higher blow

ratios. The CFD analysis indicates that the additional surface features are effective in reducing the passage vortex and providing a larger area of coolant coverage without introducing additional aerodynamic loss.

INTRODUCTION

Purge air cooling has been one of the widely used cooling techniques to protect the turbine end-wall from over-heating. In practice, one major challenge in purge air cooling is the presence of passage secondary flow vortices, which could lift the cooling air off the end-wall and result in a rapid decay in cooling performance.

The contribution of passage vortex to the total aerodynamic loss in a turbine blade row can be as high as 30-50%, according to the study of Sharma and Butler [1]. A lot of research efforts have been made towards this topic over the past decades. Hawthorne [2] first proposed an end-wall vortex model, which shows the passage vortex but omitting the formation of horseshoe vortex at the leading edge. Langston et al. [3] updated the secondary flow model based on their measurement. They showed that at the inlet of the blade passage, the boundary layer separates at the blade leading edge and gives rise to the horseshoe vortex. One leg of the horseshoe vortex moves into the blade passage and travels from the pressure side to the suction side and eventually evolves into passage vortex. The other leg of the horseshoe vortex enters the adjacent passage and forms the counter vortex. Sieverding and Bosche [4] studied the development and the interaction between the passage vortex and counter vortex through smoke visualization. The understanding of multi-vortex flow organization was further advanced by Wang et al. [5] through their flow visualization.

The highly three-dimensional flow in the cascade underpins the thermal performance. Blair [6] studied the end-wall heat transfer in a vane passage and reported that the end-wall heat transfer is strongly influenced by the existence of the large vortex located in the corner between the end-wall and the suction surface. The end-wall heat transfer measurement result by the work of Graziani et al. [7] show that the heat transfer coefficient on the suction surface is influenced by the passage vortex, while the heat transfer coefficient on the pressure surface is not affected by the secondary flow. Hylton et al. [8] performed heat transfer measurement in an uncooled linear cascade end-wall, and found that the Stanton number near the blade leading edge is about three times higher than that at mid-pitch of the passage entrance. Goldstein and Spores [9] further confirmed that very high heat transfer coefficient appears near the leading edge due to the existence of horseshoe vortex. The passage vortex and corner vortex enhance the heat transfer at downstream locations. Near the trailing edge, a significant increase in heat transfer exists mainly due to the strong mixing of two flows from both sides of the blade. The effect of free stream turbulence was considered in the study of Kang and Thole [10] and Radomsky and Thole [11]. It was found that the heat transfer increases as the turbulence intensity increases.

End-wall film cooling has been studied by many researchers, including Goldman and McLallin [12], Sieverding and Wilputte [13], Freidrichs et al. [14], Han et al. [15], and Chyu [16]. All these works deliver a consensus that the secondary flow has a strong detrimental impact on film cooling on the end-wall.

Much research attention has been paid to mitigating the secondary flow. End-wall contouring is one of the passive flow control methods. Rose [17] pioneered the concept of using a non-axisymmetric end-wall profile to alter the static pressure distribution. A three-dimension end-wall profile was designed in both axial and circumferential directions. The CFD results show that the end-wall contouring leads to 70% reduction of the static pressure non-uniformities. Yan et al. [18] employed convex and concave curvature on different regions of end-wall. Their experimental and numerical results proved that 20% reduction in the pressure loss can be achieved. Harvey et al. [19] designed the non-axisymmetric end-wall by using the linear design system. The CFD results show that the exit flow overturning and underturning are largely reduced, the two legs of the horseshoe vortex are appropriately controlled by the convex and concave profile. Hartland et al. [20] and Ingram et al. [21] reported similar findings with a net secondary loss reduction of about 24% by using end-wall contouring. Saha and Acharya [22] profiled the end-wall by combining two curves which vary in the streamwise and pitchwise direction respectively. The numerical results show that the total pressure loss is lower than that in the smooth end-wall case. Praisner et al. [23] used a gradient-based optimization algorithm to design the end-wall for the low-pressure turbine. The numerical prediction shows that the non-axisymmetric endwall contouring is effective in reducing passage vortex and pressure loss. Leading edge modification is another flow control method to alter the horseshoe vortex development. Han and Goldstein [24] used fillet geometry around the blade leading edge, which removes the horseshoe vortex and reduces the heat transfer near the leading edge. Sauer and Wolf [25] employed a bulb

geometry onto an inlet guide vane. The bulb design strengthens counter vortex, which counter-acts the passage vortex. Becz et al. [26] compared both Sauer bulb and fillet configurations in a large-scale cascade. The results indicate that the large bulb geometry does not reduce total loss, while the small bulb and fillet geometries show equal area-averaged total loss reduction of 8%. The principle of end-wall fence concept was to alter the cross passage flow away from suction side by employing a single fence to the end-wall surface. Kawai [27] installed the fence with several heights on the end-wall as well as blade suction surface. The most effective control was achieved when the fence height equaled to $1/3$ of the undisturbed boundary layer thickness and placed in the middle of the blade passage. Chung et al. [28-29] used the flow visualization method and LDV measurement to study the effect of a triangular-shaped fence. The results show that the strength of the vortical motion is largely reduced by the end-wall fence, especially for the pressure side leg of the horse vortex. Latterly, Govardhan et al. [30] and Zhong et al. [31] investigated end-wall fence with different length, height, and pitch-wise installation location. The fences under investigation were also found effective in preventing the development of the horseshoe vortex filament on the pressure surface. However, the design has not been practically implemented in turbines due to the concern of being burnt out by the hot gas.

Very recently, motivated by the advances in manufacturing technology, especially Additive Manufacturing, Miao et al. [32-33] proposed a new secondary flow control technique: adding engineered surface structure onto the end-wall surface. The strength of passage vortex was found to be greatly reduced with the addition of small-scale ribs or

wavy grooves. The present study continues to investigate the feasibility of enhancing purge air cooling effectiveness through these engineered surface features. Part I of this paper presents experimental and numerical findings of cooling enhancement from a 90° turning duct, which was used as a simplified turbine passage without the horseshoe vortex. In the Part II of this paper, purge air cooling performance on the end-walls of a linear cascade with and without small-scale ribs are reported. Cooling effectiveness, **heat transfer coefficient**, and net heat flux reduction data were obtained and analyzed through transient thermal experiment in a low speed tunnel. CFD simulation using commercial code ANSYS FLUENT was also conducted **to confirm the experimental findings and further reveal the physics behind.**

EXPERIMENTAL FACILITY AND MEASUREMENT TECHNIQUES

Transient thermal measurement was conducted in a low-speed linear cascade facility shown in Fig.1. The test section contains four blades and three flow passages. Near the suction-side sidewall, two boundary layer bleeds and two movable tail-flaps were designed and adjusted to deliver a reasonable flow periodicity. The inlet test section is a rectangular cross-section with dimensions of 130 mm (W) by 80 mm (H). The inlet velocity was maintained at 20 m/s and the turbulence intensity at the test section inlet is about 1%.

The inlet boundary layer thickness was measured by using a boundary layer probe at the one chord distance upstream of the cascade inlet. The single hole probe has a flat

tip to minimize potential errors in total pressure measurement. Figure 2 shows the measured inlet velocity profile. Due to the probe wall interaction, the data was not valid within 1 mm height to the end-wall. A typical turbulent boundary layer characteristic can be observed. The Inlet boundary layer thickness and shape factor are 6mm and 1.3, respectively. The inlet total and static pressures were measured by a pitot-static probe at the same location. In the present study, the turbine blade profile is similar to the one studied by Wright et al. [34]. Details of the flow condition and blade geometry are summarized in Table 1.

A heater mesh was installed upstream of the test section to provide a step increase in mainstream flow temperature. The mesh is powered by a 100 kW DC power and raises the mainstream temperature to 345K. A zinc selenide window was flush mounted into the cascade top wall, so that the entire middle passage is within the field of view of the infrared (IR) camera.

FLIR A325 IR camera was employed in the thermal measurement. It has a spatial resolution of 320×240 pixels with a 16-bit grayscale. The IR camera is equipped with a lens of 18 mm focal length. The frequency of the IR camera is 60 Hz. An In-situ calibration of the IR camera, similar to previous research by Schulz [35], O'Dowd et al [36], and Zhang et al. [37-39], was conducted in the present study.

Two types of end-wall, smooth and ribbed were used in the experiments. On the ribbed end-wall surface, the ribs start from the rim seal exit to 55% chord downstream of the blade leading edge. The inter-changeable end-wall was made by 3D printing and the

material has a very low thermal conductivity. The rib array geometry is summarized in Table 2.

The purge air system is similar to the one used in the Part I paper. The cooling air of 293 K is supplied through a vortex tube, and the flow rate was measured by a digital flow meter. A thermocouple is attached **inside the cavity**. The cooling flow enters the wind tunnel through a labyrinth-like rim seal. Detailed geometry of the rim seal is also shown in Fig.1. This rim seal design prevents ingestion of the hot mainstream gases into the engine cavity and accurately represents the stator-rotor rim seals in real turbine. The rim seal is located $22.7\% C_x$ upstream of the blade leading edge and covered a width of 1.5 blade passages. The slot dimensions and flow conditions are same as the experiment of **Wright and Han [34]**. **Three purge air blowing ratios (0.7, 1.0, and 1.3) were studied.**

Transient thermal measurement technique was used in the present study. **Figure 3a** presents the time histories of the cold purge air, end-wall and inlet temperatures during a typical transient experiment. After a step heating by the heater mesh, the mainstream temperature (red color) and the temperature of cold purge air (blue color) were maintained at a relatively constant value for a short period of time.

For an established flow field near the end-wall surface, the heat transfer coefficient can be defined as,

$$q'' = h(T_{ad} - T_w) \quad (1)$$

where q'' is the heat flux, T_{ad} is adiabatic wall temperature, T_w is end-wall temperature. For the solid side, it is reasonable to assume one dimensional semi-infinite conduction due to the low conductivity material employed for the end-wall surface. The

local heat flux can be calculated directly based on the transient wall temperature history and material thermal properties. In this study, a well-established Impulse Response Method, developed by Oldfield [40] and further implemented by a series of research by O'Dowd et al. [36], Zhang et al. [37-39], and Ma et al [41], was employed. This method uses discrete deconvolution and a pair of nonsingular analytical solutions to the convective heat transfer equation to derive a digital filter impulse response, then the heat flux can be determined from temperature traces based on the convolution integral. The measured thermal product $\sqrt{\rho C \kappa}$ of the end-wall material is $564 \sqrt{s/m^2K}$ (previously reported by Ma et al [41]).

Figure 3b shows the time history of local heat flux (calculated) and wall temperature (measured) for a sample location on the end-wall during one transient measurement. Both heat flux and temperature values were non-dimensionalized. All the data points in Fig. 3b follow a linear trend, which indicates and proves the validity of the convection equation (1) and establishment of the flow field during the transient experiments. Both heat transfer coefficient and adiabatic wall temperature can be obtained from linear regression: the slope of the regression line is the Nusselt number and the x-axis interception is the adiabatic wall temperature.

However, the semi-infinite 1-D conduction is a poor assumption near all the corners of the ribs as lateral conduction (mostly 2D) effects dominate (O'Dowd et al. [36] and Jiang et al. [42]). In the present study, a case study on 2D transient conduction analysis was conducted to assess the errors for the near-rib region if the 1D conduction is still assumed to process the surface temperature trace. A detailed description of similar

practice can be found in Jiang et al. [42]. Figure 4 shows the temperature contour within the solid three seconds after the ribbed wall is suddenly exposed to convection with a typical constant heat transfer coefficient value and fluid driving temperature (70 w/m²K and 345 K, respectively, in the present experiments). The Impulse Response method is employed next to calculate the heat flux history based on the semi-infinite 1D assumption and the complete temperature trace during the transient heating history. The percentage differences between the calculated values and the specified heat transfer coefficient (true value) is shown in Fig. 4. The 1D conduction assumption is proved to be reasonable for locations at the central region of rib groove, which covers about 60% of the ribbed surface area. As expected, the solution shows an overestimated heat transfer coefficient with an error over 10 percent near the corner. The semi-infinite assumption is absolutely not valid for rib top surface (over 110% error). Therefore, data shown on the rib top surface and groove corner regions can only be cautiously examined for their qualitative trend.

EXPERIMENTAL UNCERTAINTY

A jitter analysis described by Moffat [43] was used to determine the overall uncertainty in the experimental study. The sources of experimental uncertainty include measured wall temperature, material properties, the calibration of the IR camera, mainstream and coolant temperature variations and measurement, etc. For transient thermal measurement and the Impulse method employed in the present work, the linear regression error also needs to be considered. A coefficient of determination R^2 , defined by Devore [44], is calculated to assess the linear regression performance. Figure 5a

presents a detailed distribution of R^2 in the measurement area for the smooth end-wall case. For the majority of the measurement region, R^2 is well above 0.9.

The 95% confidence level was used to estimate the uncertainty in the transient thermal measurement. Four repeated transient tests were taken for each type of end-wall surface. Figure 5b shows the contour of relative uncertainty in adiabatic wall temperature. The relative uncertainty in T_{ad} is below 0.5% for most of the test surface.

In the present experimental study, the element systematic error sources mainly come from the wall temperature measurement and the determination of end-wall material property (also reported previously by O'Dowd et al. [36]). A summary of uncertainty values for various measurement properties is presented in Table 3.

COMPUTATIONAL DETAILS AND VALIDATION

Steady Reynolds-Averaged Navier-Stokes (RANS) simulation was performed by using ANSYS FLUENT software. The $k-\omega$ shear stress transport (SST) turbulence model was selected to model the turbulence. The computational domain is shown in Fig. 6, which includes one blade with periodic boundary conditions, rim seal and purge air cavity. The blade profile, flow angle and inlet boundary conditions are the same as the experiment setup. The temperatures at cascade inlet and purge air inlet were set as 345 and 293K, respectively, according to the thermocouple measurements. The duct outlet boundary condition was specified as ambient pressure. Isothermal boundary conditions with two different temperatures, namely 300 K and 310 K, are applied on the end-wall for the derivation of convective heat transfer coefficient and adiabatic wall temperature. This

two-point method is based on the assumption that the flow field is independent of the temperature boundary condition within the range of the two isothermal values.

The flow domain shown in Fig. 6 is discretized with fully structured hexahedra mesh created by using Pointwise software. The grids in the purge air rim seal and around the ribs are also shown in Fig. 6. The total grid size is about 5 million cells and the y^+ on the end-wall is in the range of 1-2. The blade pitch is used as the length scale for non-dimensionalization. Three grid sizes were studied to check the grid independence. The grid of 5 million cells was chosen for further analysis, considering the heat flux value is not changed with larger grid density. Visualization of the CFD results was accomplished by using a commercial software Enight.

The simulation strategy employed in this paper was validated against benchmarking experimental data previous by Wright et al. [45] in a linear cascade. Same experimental boundary conditions and turbine cascade dimension are employed in the CFD simulation. Figure 7 shows the end-wall film cooling effectiveness distributions from both experiment and CFD. The overall agreement is satisfactory. The coolant in CFD prediction is less diffused than in experiment, which is a typical performance behavior for a standard RANS solver. The interaction between secondary flow and cooling fluid needs to be better resolved by CFD solvers with high-fidelity, such as LES. Results in Figs 6a and 6b consistently indicate that the purge air is quickly swept to the blade suction side after injection through the slot and there is a poor coverage near the pressure side surface.

Note that the CFD data in Fig. 6 are only for benchmarking comparison. There is a slight difference in purge air slot location between Wright et al. [34] and Wright et al. [45]. Results presented next are from a configuration similar to Wright et al. [34].

RESULTS AND DISCUSSIONS

Experimental data of cooling effectiveness, heat transfer coefficient, and Net Heat Flux Reduction, for different purge air blowing ratios (BR=0.7, 1., 1.3) are firstly presented in this session. The case for BR=1.0 was selected for further comparison with CFD and detailed analysis. The flow physics associated with the end-wall ribs are discussed, together with design optimization strategy and potential applications.

Figure 8 presents film cooling effectiveness η measured on the smooth and ribbed surface for different blowing ratios. The film cooling effectiveness is calculated from:

$$\eta = \frac{T_{\infty} - T_{ad}}{T_{\infty} - T_c} \quad (2)$$

where T_c is the cold purge air temperature, T_{∞} is the mainstream temperature, and T_{ad} is the adiabatic wall temperature.

In Fig. 8, a consistent enhancement in cooling effectiveness from the ribbed end-wall cases can be observed by comparing to the results from the smooth cases. At all three blowing ratios. Aligned by the small ribs, the cooling purge air is allowed to penetrate further downstream and provide a much large coverage area. The higher effectiveness with higher blower ratio is well-expected. However, for the cases with relatively lower BRs, the film cooling effectiveness value is still low around the near pressure side region (especially for BR=0.7), which indicates a poor coverage by the coolant around the ribbed

surface due to insufficient cooling flow rate. Apparently, for a specific blowing ratio, further design optimization of the surface structure is needed to avoid their direct contact with the hot gas. As discussed in Part I of this paper, it is not possible to fully stop the radial migration of the purge air flow. This ribbed end-wall concept should be combined to conventional film cooling (or effusion cooling) in practice.

Figure 9 shows the distributions of heat transfer coefficient ratio $\frac{h_f}{h_0}$ for cases with three blowing ratios, where h_f is heat transfer coefficient measured with purge air flow, and h_0 represents heat transfer coefficient without purge air flow for smooth end-wall. High heat transfer coefficient ratio occurs near the exit of the purge air rim seal slot for all the cases. Adding ribs increases the local heat transfer coefficient. An important message from Fig. 9 is that, if this enhancement cannot be balanced out by a good level of cooling effectiveness, there will be no benefit from ribbed end-wall design.

Net Heat Flux Reduction (NHFR), previously defined by Sen et al. [46], has been widely used by to assess the combined outcome of the changes in film cooling effectiveness and heat transfer coefficient. The NHFR is defined as below:

$$NHFR = 1 - \frac{h_f}{h_0} (1 - \eta\varphi) \quad (3)$$

φ is the non-dimensional metal temperature, which is dependent on the metal conductivity and internal cooling technology. The definition of φ is:

$$\varphi = \frac{T_\infty - T_c}{T_r - T_b} \quad (4)$$

where T_∞ is the mainstream temperature, T_c is the coolant total temperature, T_b is the blade metal temperature, T_r is the recovery temperature. For a typical operational film cooled turbine blade, a value of 1.6 is used based on the work of Sen et al. [46].

For end-wall region with ribs, the heat load introduced by additional surface area needs to be taken into account. To fully assess the performance of ribbed structure, a Net Heat Load Reduction (NHLR) is defined as,

$$NHLR = 1 - \frac{\int_{A_f} h_f (T_{ad} - T_w) dA_f}{\int_{A_0} h_0 (T_\infty - T_w) dA_0} = 1 - \frac{\int_{A_f} h_f \left(\frac{T_{ad}}{T_w} - 1 \right) dA_f}{\int_{A_0} h_0 \left(\frac{T_\infty}{T_w} - 1 \right) dA_0} \quad (5)$$

where the temperature ratios T_∞/T_w , and T_{ad}/T_w can be replaced by typical values at engine conditions. The NHLR definition can be further simplified as follows:

$$NHLR = 1 - \frac{\int_{A_f} h_f (1 - \eta\phi) dA_f}{\int_{A_0} h_0 dA_0} \quad (6)$$

Due to the experimental errors near the small ribs and lack of information from the rib side walls, it is not possible to estimate and compare experimental NHLR values. NHLR data can only be assessed based CFD data discussed next.

The distributions of NHFR based on experimental data are still presented in Fig. 10 to illustrate the local performance over the projected end-wall wall. For the BR=1.0 and 1.3 cases, significant NHFR enhancement by ribbed surface can be observed near the purge air entry region as well as the further downstream area. This is mostly due to the improved cooling effectiveness shown in Fig. 8. It can be expected that the overall cooling

needs from the downstream end-wall region should be greatly reduced. On the other hands, the benefit of ribbed surface for BR=0.7 case is less obvious. There are some enhancements from the ribs near the suction side region, however a large amount of ribbed surface area is exposed to the hot gas due to low cooling flow supply. The rib geometry needs to be carefully optimized to suit the operational range of purge air blowing ratio.

In addition, the overall improvement is less significant compared with the results reported in Part I paper for a simplified curved channel, which can be attributed to the detrimental effect from the strong horseshoe vortex.

Next, CFD results for BR=1.0 case are presented, and the detailed flow structure and aerodynamic performance are discussed.

Figures 11, 12, and 13 presents CFD results of the film cooling effectiveness, heat transfer coefficient ratio $\frac{h_f}{h_o}$, and NHFR, respectively. Overall a good qualitative agreement can be observed in comparison with the experimental results shown in Figs 8-10. Quantitatively, there are discrepancies between experimental and CFD results. Similar to the performance shown in Part I paper, the RANS CFD results are less diffused than the measurement data. The complex interactions between horseshoe vortex, passage vortex, and end-wall ribs needs to be better resolved by CFD solvers with high-fidelity (such as LES).

For BR=1.0 case, the overall Net Heat Load Reduction (NHLR) based on all the exposed surface area of the ribbed end-wall only has a marginal 2% improvement over the smooth

case. More improvement on NHLR is expected for the BR=1.3 case based on the observations in Figs. 10e and 10f. It seems that, instead of reducing the global heat load, the benefit of ribbed end-wall is on spreading the coolant to a much wider end-wall area. Potentially additional film cooling might not be needed for some further downstream region. There should also be a large design space to optimize the rib structure to gain further enhancement in NHLR (as discussed in Part I paper).

The vortices developing in the turbine blade passage with and without ribbed surface structure are visualized through Q-criterion, as shown in Fig. 14. The end-wall surface is colored by the film cooling effectiveness η . Over the smooth surface (Fig. 10a), the low momentum boundary layer fluids separates at the blade leading edge and develops into the horseshoe vortex, which splits into two legs. One leg of the horseshoe vortex develops over the blade suction surface and eventually joins the passage vortex. The purge air injected through the rim seal is merged within the pressure side of horseshoe vortex and swept to suction side quickly. This is consistent with the film cooling effectiveness contour on end-wall surface. Figure 14b shows the horseshoe vortex is greatly modified by the ribbed surface. The strength of suction side leg of horseshoe vortex is much reduced, so as the passage vortex developed further downstream.

To visualize the coolant coverage over the end-wall, an iso-temperature surface with non-dimensional fluid temperature $\theta = 0.6$ is shown in Fig. 15. θ is defined as:

$$\theta = \frac{T - T_c}{T_\infty - T_c}$$

where T_c is the cold purge air temperature, T_∞ is the mainstream temperature and T is local fluid temperature. Lower θ value indicates a colder local fluid temperature, thus θ

is also an indication of the purge air concentration. Figure 15a clearly shows the injected purge air is swept towards the blade suction side due to the strong pressure gradient. With the addition of rib structures on the surface, the purge air cannot be immediately swept towards the suction side, instead, it follows the streamlined ribs, and remains close to the end-wall surface for a longer distance, resulting in a larger coverage over the end-wall.

The distribution of non-dimensional fluid temperature θ within three cross-sections along the blade passage is shown in Fig. 16. The three cross-sectional planes are located at 20%, 50% and 65% chord from the leading edge. As revealed in Fig. 16, the low temperature air tends to accumulate onto the suction side for both cases. At the 65% C_x plane of the smooth end-wall case, the cold air has been lifted off the wall and are contained in the passage vortex. For the ribbed surface case, most purge air concentration spreads wider in the pitchwise direction while stays closer to the end-wall and occupy the rib channels at 20% and 50% C_x cross sections. Compared with the smooth case, the near wall temperature in ribs surface passage is much lower.

The streamwise vorticity in the three cross planes at 20%, 50% and 65% C_x are presented in Fig. 17 to reveal the evolution of the secondary flow. The streamwise vorticity is calculated as

$$\Omega_s = \Omega_x \cos \beta_{mid} + \Omega_y \sin \beta_{mid},$$

where β_{mid} is the relative angle between the local blade camber angle and x -axis in midspan. The streamwise vorticity is further non-dimensionalized by C_x/V_∞ . The negative

vorticity (red in color) is associated with the secondary vortex, while the positive vorticity (blue in color) represents the vortex with an opposite rotation.

For the case with smooth end-wall, as the flow is turning, the passage vortex which has negative streamwise vorticity develops and moves quickly across the passage. It accumulates in the suction surface and end-wall corner at 65% C_x . While in the ribbed case, the strength of passage vortex is largely reduced by the blockage effect of ribs. The ribs also introduce vorticity with an opposite sign, which have been revealed as vortices of smaller scale than the passage vortex. Two zoomed in pictures are also shown in Fig. 17b to illustrate the detailed flow development over these ribs. The black lines indicate the secondary streamlines projected to the cross plane. Due to the occupation of the positive vorticity, the cross flow cannot follow the ribs curvature well and an earlier lift-off of the streamlines can be observed. These flow structures are consistent and similar to previous findings by Miao et al. [33].

Figure 18 shows contours of dimensionless entropy generation rate per unit volume at three axial planes. As proposed by Denton [47], the entropy generation rate per unit volume is given by

$$T\dot{S}_{vol} = \frac{\tau dV}{dn} + \frac{\lambda \left(\frac{dT}{dn}\right)^2}{T}$$

In Fig. 18, the value of $T\dot{S}_{vol}$ normalized by $\rho_e V_e^3 / C_x T_e$. As expected, high entropy generation rate region is associated suction side and end-wall surfaces for both cases. But there are apparent differences which are interesting to compare in detail. The stronger passage vortex rolling up over the smooth end-wall reveals itself by a local region with

relatively higher entropy generation rate, as shown in Fig. 18a. For the ribbed end-wall case in Fig. 19b, higher entropy generation rate produced by the friction of rib surfaces is shown in-between and on top of the ribs. This additional entropy generation due to friction balances the benefit from the reduction of passage vortex. When the purge air exits the rib grooves, a higher rate region occurs due to the mixing loss at 65% C_x .

Figure 19 presents the distributions of aerodynamics loss coefficient at the exit plane of the blade passage. The aerodynamics loss coefficient is defined as

$$\zeta = 1 - \frac{(\dot{m}_c \cdot C_{p,c} \cdot T_{0,c} + \dot{m}_{in} \cdot C_{p,in} \cdot T_{0,in}) \left(1 - \left(\frac{P}{P_0}\right)^{\frac{\gamma-1}{\gamma}}\right)}{\dot{m}_{in} \cdot C_{p,in} \cdot T_{0,in} \cdot \left(1 - \left(\frac{P_{mid}}{P_{0,in}}\right)^{\frac{\gamma-1}{\gamma}}\right)_{in} + \dot{m}_c \cdot C_{p,c} \cdot T_{0,c} \cdot \left(1 - \left(\frac{P_{mid}}{P_{0,c}}\right)^{\frac{\gamma-1}{\gamma}}\right)_c}$$

The difference between smooth and ribbed cases in aerodynamic loss is within 2%, which is negligible considering the numerical accuracy of the RANS calculations. For the ribbed end-wall, there is a trade-off between the additional mixing loss due to more coolants brought to further downstream and the weakened passage vortex. Further experimental investigation is needed to confirm this numerical observation.

SUMMARY AND CONCLUSIONS

The present study investigates a novel design methodology to improve purge air cooling effectiveness by engineered end-wall surface structure in a linear turbine cascade environment. Both results from transient thermal measurements and CFD analysis are

presented to demonstrate the feasibility of the concept and the working mechanism behind.

Similar to the findings from the simplified turning duct study in the Part I paper, it has been consistently observed that adding small ribs is able to reduce the horseshoe vortex and passage vortex and provide favorable alignment to the cooling flow. The purge air flow is found to cover a much larger area over the turbine end-wall. The enhancement in cooling effectiveness is significant for purge air blowing ratio $BR=1.0$ and $BR=1.3$. CFD results for $BR=1$ case show that there is no additional overall heat load introduced by the increased surface area, and the additional aerodynamic penalty introduced by the small ribs is negligible.

It is suggested that the surface feature should be optimized according to purge air blowing ratio, blade loading, incoming flow boundary layer characteristics, etc. It should be combined with conventional film cooling technique in practical design. Following the similar flow control mechanism, small-scale surface feature can also be applied to other aspects in turbomachinery, such as the exit region of film cooling holes and internal cooling channels. The extra design space and flexibility offered by the advances in Additive Manufacturing deserves more attention for future aero-thermal research.

NOMENCLATURE

C_x	Axial chord
d	Rib distance
EXP	Experiment
h	Rib height, Heat transfer coefficient (W/(m ² -K))
IR	Infrared
\dot{m}	Mass flow rate
n	Rib number
P	Pitch, Pressure
PS	Pressure side
$RANS$	Reynolds-Averaged Navier-Stokes
R^2	Coefficient of determination
S	Span
SS	Suction side
T	Local temperature
T_{ad}	Adiabatic wall temperature
T_b	Blade metal temperature
T_p	Purge air temperature

T_r	Recovery temperature
T_w	End-wall temperature
T_∞	Mainstream temperature
V_∞	Inlet velocity
w	Rib width
Y/P	Pitch-wise measurement location normalized by pitch
y^+	Non-dimensional wall distance: $y^+ \equiv u_\tau y/\nu$
Z/S	Span-wise measurement location normalized by span
$NHFR$	Net heat flux reduction
$NHLR$	Net heat load reduction $NHLR = 1 - \frac{\int_{A_f} h_f(1-\eta\varphi)dA_f}{\int_{A_0} h_0 dA_0}$
β	Pitch angle
θ	Non-dimensional fluid temperature
δ	Boundary layer thickness
φ	Non-dimensional metal temperature
η	Film cooling effectiveness
Ω	Vorticity

REFERENCES

- [1] Sharma, O., and Butler, T., 1987, "Predictions of End-wall Losses and Secondary Flows in Axial Flow Turbine Cascades," *ASME J. Turbomach.*, 109, pp. 229-236.
- [2] Hawthorne, W. R., 1955, "Rotational Flow through Cascades," *The Quarterly Journal of Mechanics and Applied Mathematics*, 8(3), 266-292.
- [3] Langston, L.S., 1980, "Crossflows in a Turbine Cascade Passage," *ASME J. of Engineering for Power*, Vol. 102, pp. 866-874.
- [4] Sieverding, C., and Bosche, V. D., 1983, "The use of colored smoke to visualize secondary flows in a turbine-blade cascade," *Journal of Fluid Mechanics*, Cambridge University Press, 134, pp. 85-89.
- [5] Wang, H. P., Olson, S. J., Goldstein, R. J., and Eckert, E. R. G., 1997, "Flow Visualization in a Linear Turbine Cascade of High Performance Turbine Blades," *ASME J. Turbomach.*, 119, pp. 1-8.
- [6] Blair, M.F., 1974, "An experimental study of heat transfer and film cooling on large-scale turbine endwalls," *ASME J. Heat Transfer*, 96(4), pp.524-529.
- [7] Graziani, R.A., Blair, M.F., Taylor, J.R. and Mayle, R.E., 1980, "An experimental study of endwall and airfoil surface heat transfer in a large scale turbine blade cascade," *Journal of Engineering for Power*, 102(2), pp.257-267.
- [8] Hoylton, L.P., Mihelc, M.S., Turner, E.R. and York, R.E., 1981, "Experimental Investigation of Turbine Endwall Heat Transfer," *AFWAL-TR-81-2077*, Vols. 1-3.
- [9] Golstein, R.J. and Spores, R.A., 1988, "Turbulent Transport on the Endwall in the Region between Adjacent Turbine Blades," *ASME J. of Heat Transfer*, Vol. 110, pp. 862-869.
- [10] Kang, M.B. and Thole, K.A., 1999, "Flow field Measurements in The Endwall Region of A Stator Vane," *ASME Paper 99-GT-188*.

[11] Rodamsky, R.W. and Thole, K.A. 2000, "High Freestream Turbulence Effects on Endwall Heat Transfer for a Gas Turbine Stator Vane," ASME Paper 2000-GT-0201.

[12] Goldman, L.J. and McLallin, K.L., 1977, "Effect of Endwall Cooling on Secondary Flows in Turbine Stator Vanes," AGARD CP-214.

[13] Sieverding, C.H. and Wilputte, Ph., 1981, "Influence of mach Number and End Wall Cooling on Secondary Flows in a Straight Nozzle Cascade," ASME J. Engineering for Power, Vol. 103, pp. 257–264.

[14] Friedrichs, S., Hodson, H.P. and Daws, W.N., 1996, "Distribution of Film-Cooling Effectiveness on a Turbine Endwall Measured Using Ammonia and Diazo Technique," ASME J. of Turbomachinery, Vol. 118, pp. 613–621.

[15] Han, J.C., Dutta, S., and Ekkad, S.V., 2000, Gas Turbine Heat Transfer and Cooling Technology, Taylor and Francis, New York, 646 pages.

[16] Chyu, M.K., 2001. Heat Transfer Near Turbine Nozzle Endwall. Annals of the New York Academy of Sciences, 934(1), pp.27-36.

[17] Rose, M., 1994, "Non-axisymmetric end-wall profiling in the HP NGV's of an axial flow gas turbine," ASME Paper No. 94-GT-249.

[18] Yan, P. J., Gregory-Smith, D. G., and Walker, P. J., 1999, "Secondary Flow Reduction in a Nozzle Guide Vane Cascade by Non-Axisymmetric End-wall Profiling," ASME Paper No. 99-GT-339.

[19] Harvey, N. W., Rose, M. G., Taylor, M. D., Shahpar, S., Hartland, J., and Gregory-Smith, D. G., 2000, "Non axisymmetric Turbine End Wall Design: Part I: Three-Dimensional Linear Design System," ASME J. Turbomach., 122(2), pp. 278-285.

[20] Hartland, J. C., Gregory-Smith, D. G., Harvey, N. W., and Rose, M. G, 2000, "Non axisymmetric Turbine End Wall Design: Part II – Experimental Validation," ASME J. Turbomach., 122(2), pp. 286-293.

[21] Ingram, G., Gregory-Smith, D., Rose, M., Harvey, N., and Brennan, G., 2002, "The Effect of End-wall Profiling on Secondary Flow and Loss Development in a Turbine Cascade," ASME Paper No. GT2002-30339.

[22] Saha, A. K., and Acharya, S., 2006, "Computations of Turbulent Flow and Heat Transfer through a Three Dimensional Non-Axisymmetric Blade Passage," ASME Paper No. GT2006-90390.

[23] Praisner, T. J., Allen-Bradley, E., Grover, E. A., Knezevici, D. C., and Sjolander, S. A., 2007, "Application of Non-Axisymmetric End-wall Contouring to Conventional and High-Lift Turbine Airfoils," ASME Paper No. GT2007-27579.

[24] Han, S. and Goldstein, R.J., 2005, "Influence of Blade Leading Edge Geometry on Turbine Endwall Heat (Mass) Transfer," ASME Paper No. GT2005-68590.

[25] Sauer, H., Muller, R., and Vogeler, K., 2001, "Reduction of Secondary Flow Losses in Turbine Cascades by Leading Edge Modifications at the End-wall," ASME J. Turbomach., 123(2), pp. 207-213.

[26] Becz, S., Majewski, M. S., and Langston, L. S., 2004, "An Experimental Investigation of Contoured Leading Edges for Secondary Flow Loss Reduction," ASME Paper No. GT2004-53964.

[27] Kawai, T., 1994, "Effect of combined boundary layer fences on turbine secondary flow and losses," JSME International Journal Series B Fluids and Thermal Engineering, 37(2), pp.377-384.

[28] Chung, J. T., Simon, T. W., and Buddhavarapu, J., 1991, "Three-Dimensional Flow near the Blade/End-wall Junction of a Gas Turbine: Application of a Boundary Layer Fence," ASME Paper No. 91-GT-45.

[29] Chung, J.T. and Simon, T.W., 1993, "Effectiveness of the gas turbine endwall fences in secondary flow control at elevated freestream turbulence levels," ASME Paper No. 93-GT-051.

[30] Govardhan, M., Rajender, A., and Umang, J. P., 2006, "Effect of Streamwise Fences on Secondary Flows and Losses in a Two-Dimensional Turbine Rotor Cascade," J. Thermal Sciences, 15(4), pp. 296-305.

[31] Zhong, J., Han, J.A., Liu, Y. and Tian, F., 2008, "Numerical simulation of endwall fence on the secondary flow in compressor cascade," ASME Paper No. GT2008-50888.

[32] Miao, X., Zhang, Q., Atkin, C. and Sun, Z., 2016, "End-Wall Secondary Flow Control Using Engineered Residual Surface Structure," ASME Paper No. GT2016-57347

[33] Miao, X., Zhang, Q., Wang, L., Jiang, H., & Qi, H, 2015, "Application of riblets on turbine blade endwall secondary flow control," Journal of Propulsion and Power, 31(6), 1578-1585.

[34] Wright, L.M., Blake, S.A. and Han, J.C., 2008, "Film cooling effectiveness distributions on a turbine blade cascade platform with stator-rotor purge and discrete film hole flows," *Journal of Turbomachinery*, 130(3), p.031015.

[35] Schulz, A., 2000, "Infrared Thermography as Applied to Film Cooling of Gas Turbine Components." *Measurement Science and Technology*, vol. 11, no. 7, pp. 948.

[36] O'Dowd, D.O., Zhang, Q., He, L., Ligrani, P.M. and Friedrichs, S., 2011, "Comparison of heat transfer measurement techniques on a transonic turbine blade tip," *Journal of Turbomachinery*, 133(2), p.021028.

[37] Zhang, Q., He, L., Wheeler, A.P.S., Ligrani, P.M. and Cheong, B.C.Y., 2011, "Overtip shock wave structure and its impact on turbine blade tip heat transfer," *Journal of Turbomachinery*, 133(4), p.041001.

[38] Zhang, Q., O'Dowd, D.O., He, L., Oldfield, M.L.G. and Ligrani, P.M., 2011, "Transonic Turbine Blade Tip Aerothermal Performance with Different Tip Gaps—Part I: Tip Heat Transfer," *Journal of Turbomachinery*, 133(4), p.041027.

[39] Zhang, Q., He, L., Cheong, B.C.Y. and Tibbott, I., 2013, "Aerothermal performance of a cooled winglet at engine representative Mach and Reynolds numbers," *Journal of Turbomachinery*, 135(1), p.011041.

[40] Oldfield, M.L., 2008. Impulse response processing of transient heat transfer gauge signals. *Journal of Turbomachinery*, 130(2), p.021023.

[41] Ma, H., Zhang, Q., He, L., Wang, Z. and Wang, L., 2017, "Cooling Injection Effect on a Transonic Squealer Tip—Part I: Experimental Heat Transfer Results and CFD Validation," *Journal of Engineering for Gas Turbines and Power*, 139(5), p.052506.

[42] Jiang, H., Chen, W., Zhang, Q. and He, L., 2015, "Analytical-Solution Based Corner Correction for Transient Thermal Measurement," *ASME Journal of Heat Transfer*, 137(11), p.111302.

[43] Moffat, R. J., 1988, "Describing the Uncertainties in Experimental Results," *Experimental Thermal and Fluid Science*, vol. 1, pp. 3–17.

[44] Devore, J.L., 2011, "Probability and Statistics for Engineering and the Sciences," Cengage learning.

[45] Wright, L.M., Gao, Z., Yang, H. and Han, J.C., 2008, "Film cooling effectiveness distribution on a gas turbine blade platform with inclined slot leakage and discrete film hole flows," *Journal of Heat Transfer*, 130(7), p.071702.

[46] Sen, B., Schmidt, D.L., and Bogard, D.G., 1996, "Film Cooling with Compound Angle Holes: Heat Transfer", J. of Turbomachinery, Vol. 118.

[47] Denton, J.D., 1993, "Loss Mechanisms in Turbomachines," Journal of Turbomachinery, 115, p.621.

Figure Captions List

- Fig. 1 A schematic of experiment facility.
- Fig. 2 Inlet end-wall boundary layer velocity profile measured one axial chord upstream of the blade leading edge.
- Fig. 3 (a) Time histories of the cold purge air, end-wall and inlet temperatures, and (b) variations of wall heat flux and surface temperature during one typical transient measurement for one selected wall location.
- Fig. 4 Measurement errors due to 1D semi-infinite conduction assumption, assessed through a 2D transient conduction analysis.
- Fig. 5 (a) R^2 distribution for linear regression, and (b) Relative uncertainty ($\%U$) in T_{ad} distribution.
- Fig. 6 Computational domain and mesh.
- Fig. 7 Film cooling effectiveness distributions obtained by Wright et al. [45] and present CFD study.
- Fig. 8 Distributions of film cooling effectiveness. (**experimental data**)
- Fig. 9 Distributions of hf/ho . (**experimental data**)
- Fig. 10 Distributions of NHFR. (**experimental data**)
- Fig. 11 Distributions of film cooling effectiveness. (**CFD results**)
- Fig. 12 Distribution of hf/ho . (**CFD results**)
- Fig. 13 Distribution of NHFR. (**CFD results**)
- Fig. 14 Iso-surfaces of Q-criteria for smooth and ribbed surface.

- Fig. 15 An iso-temperature surface with $\theta = 0.6$
- Fig. 16 Non-dimensional temperature θ distributions at three cross sections.
- Fig. 17 Streamwise vorticity distribution at three cross sections.
- Fig. 18 Dimensionless entropy generation rate per unit volume distributions at three cross sections.
- Fig. 19 Distributions of Aerodynamic loss coefficient at the exit plane.

Table Caption List

Table 1 Flow condition of the test section and blade geometries.

Table 2 Geometry of ribs array on the end-wall.

Table 3 Measurement uncertainties

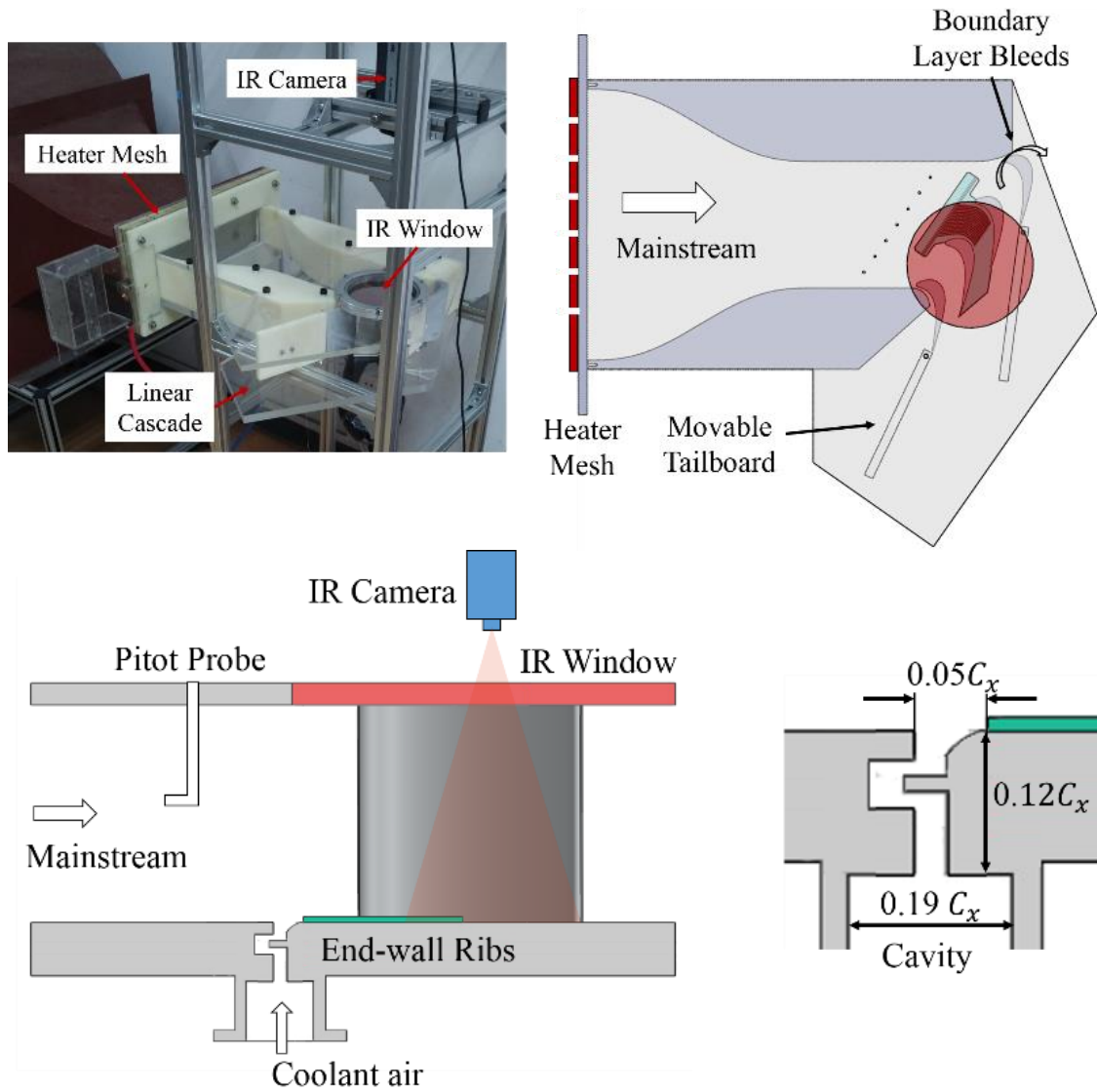


Figure 1. A schematic of experiment facility.

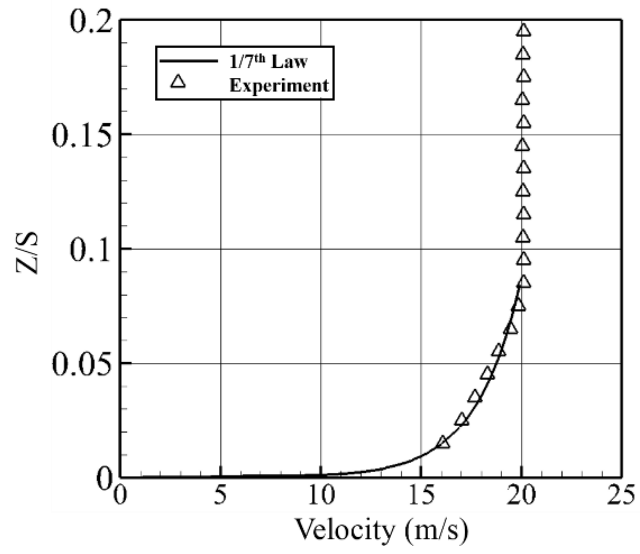


Figure 2. Inlet end-wall boundary layer velocity profile measured one axial chord upstream of the blade leading edge.

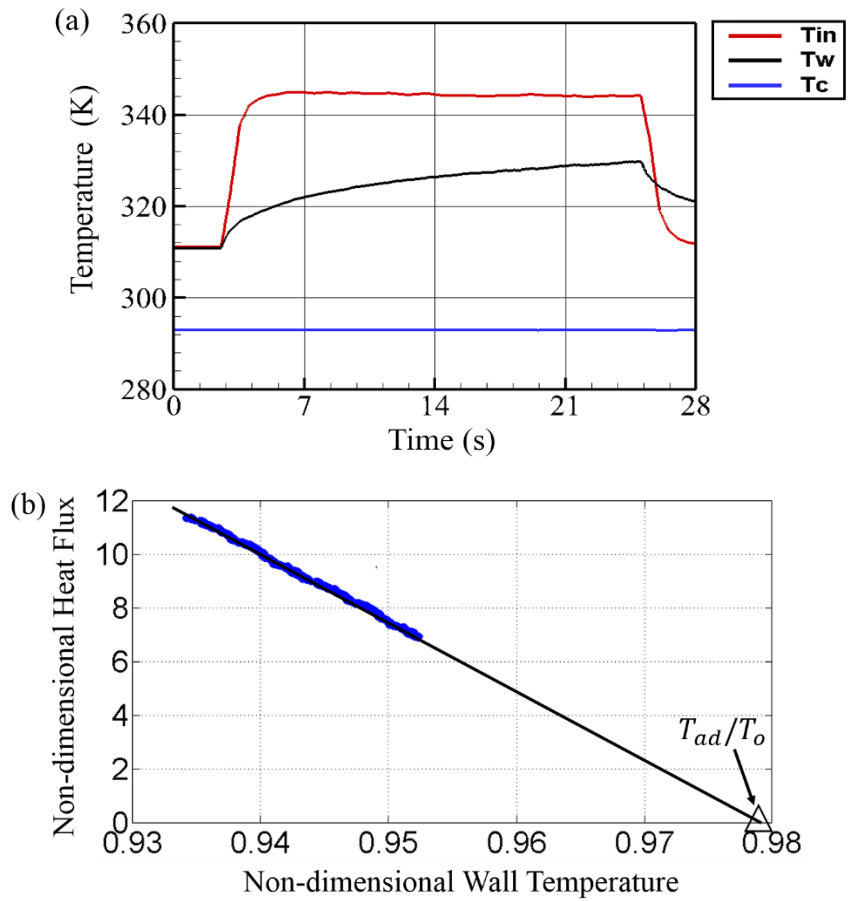


Figure 3. (a) Time histories of the cold purge air, end-wall and inlet temperatures, and (b) variations of wall heat flux and surface temperature during one typical transient measurement for one selected wall location.

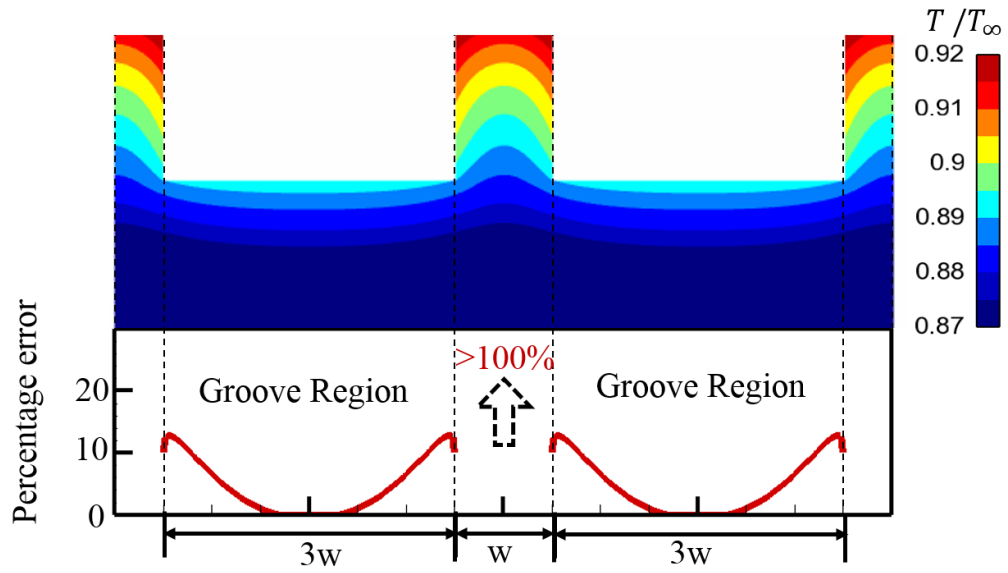


Figure 4. Measurement errors due to 1D semi-infinite conduction assumption, assessed through a 2D transient conduction analysis.

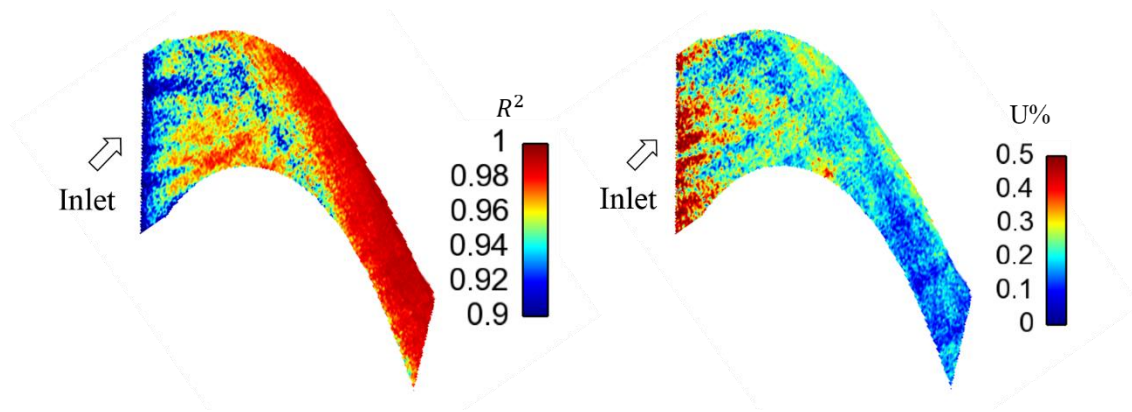


Figure 5. (a) R^2 distribution for linear regression, and (b) Relative uncertainty (U) in T_{ad} distribution.

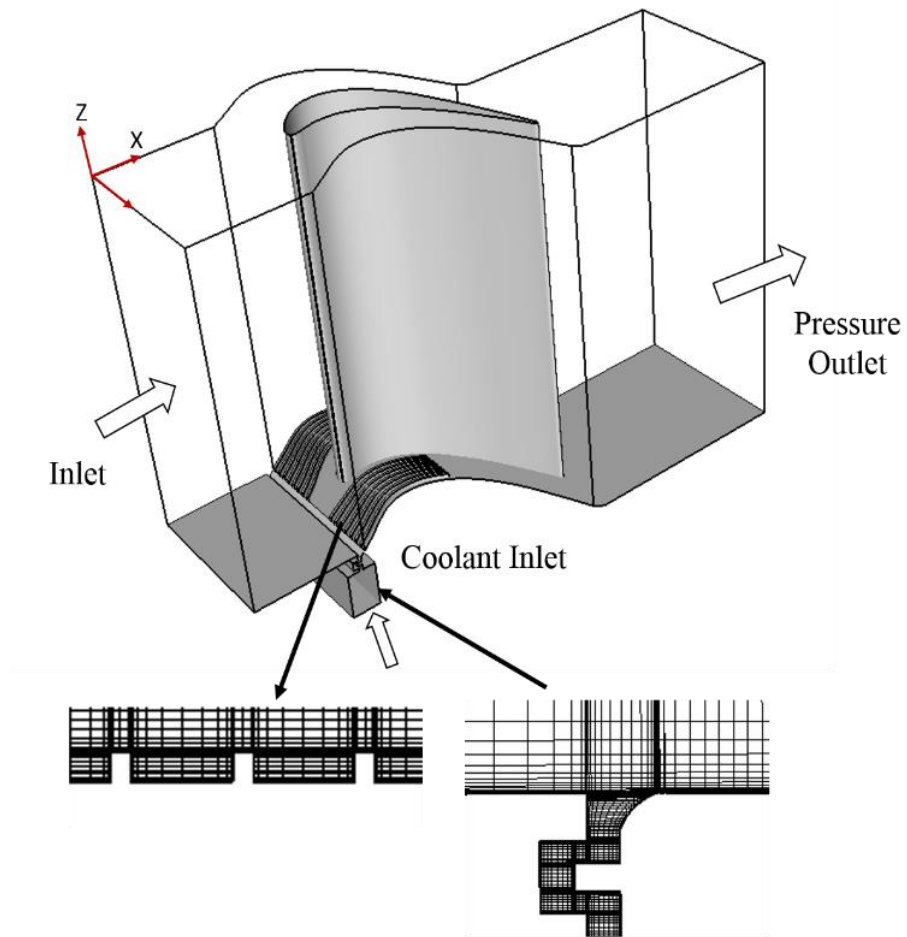
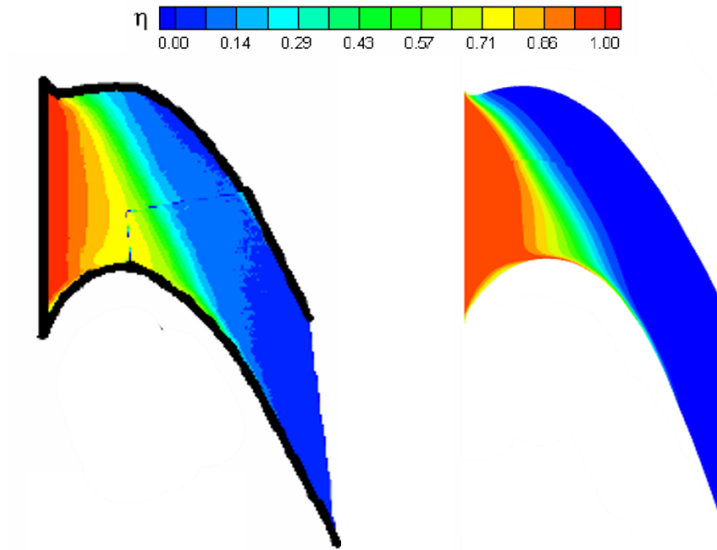


Figure 6. Computational domain and mesh.



(a) Experimental study (Wright et al. [45]) (b) CFD results from the present study

Figure 7: Film cooling effectiveness distributions obtained by Wright et al. [45] and present CFD study.

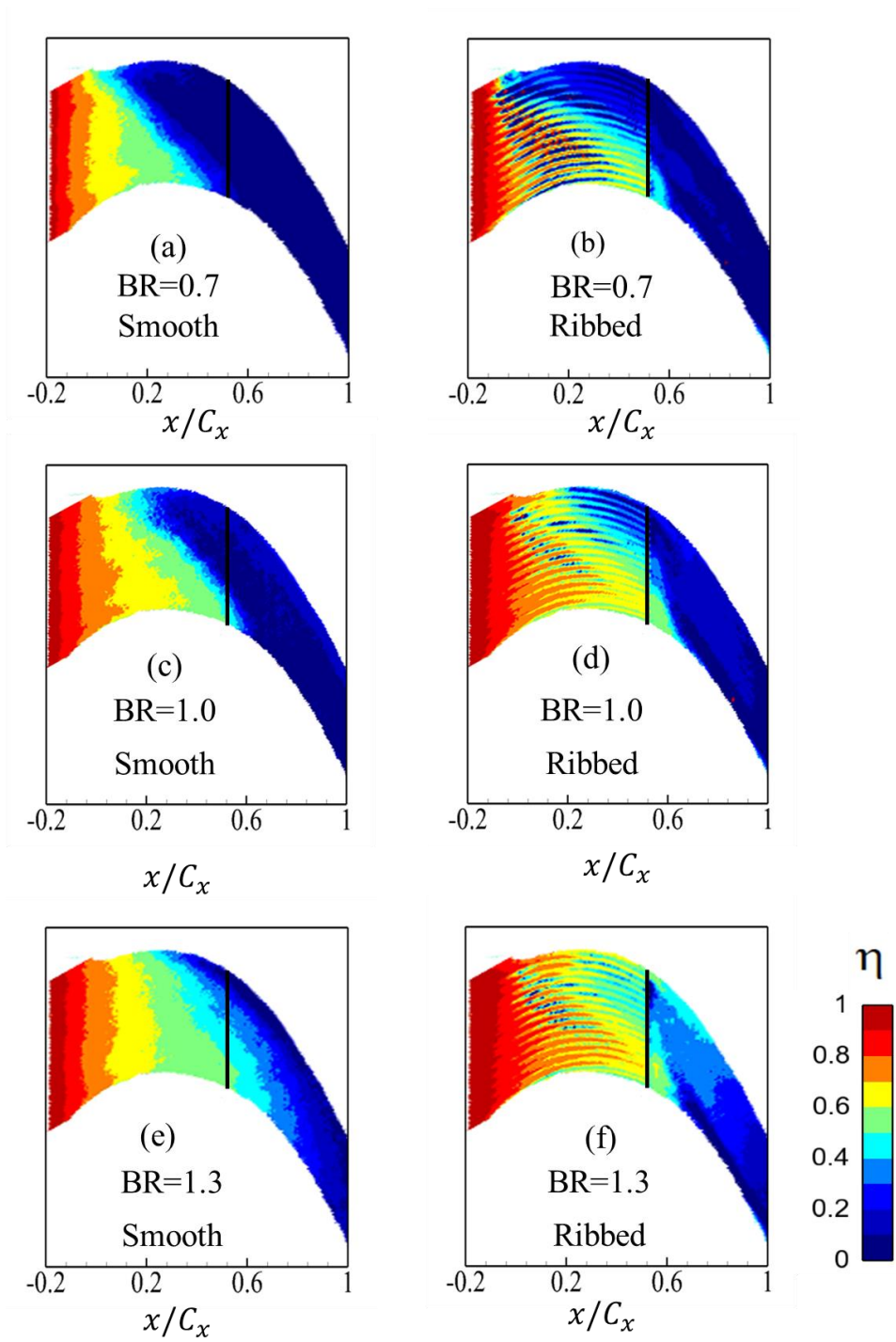


Figure 8. Distributions of film cooling effectiveness. (experimental data)

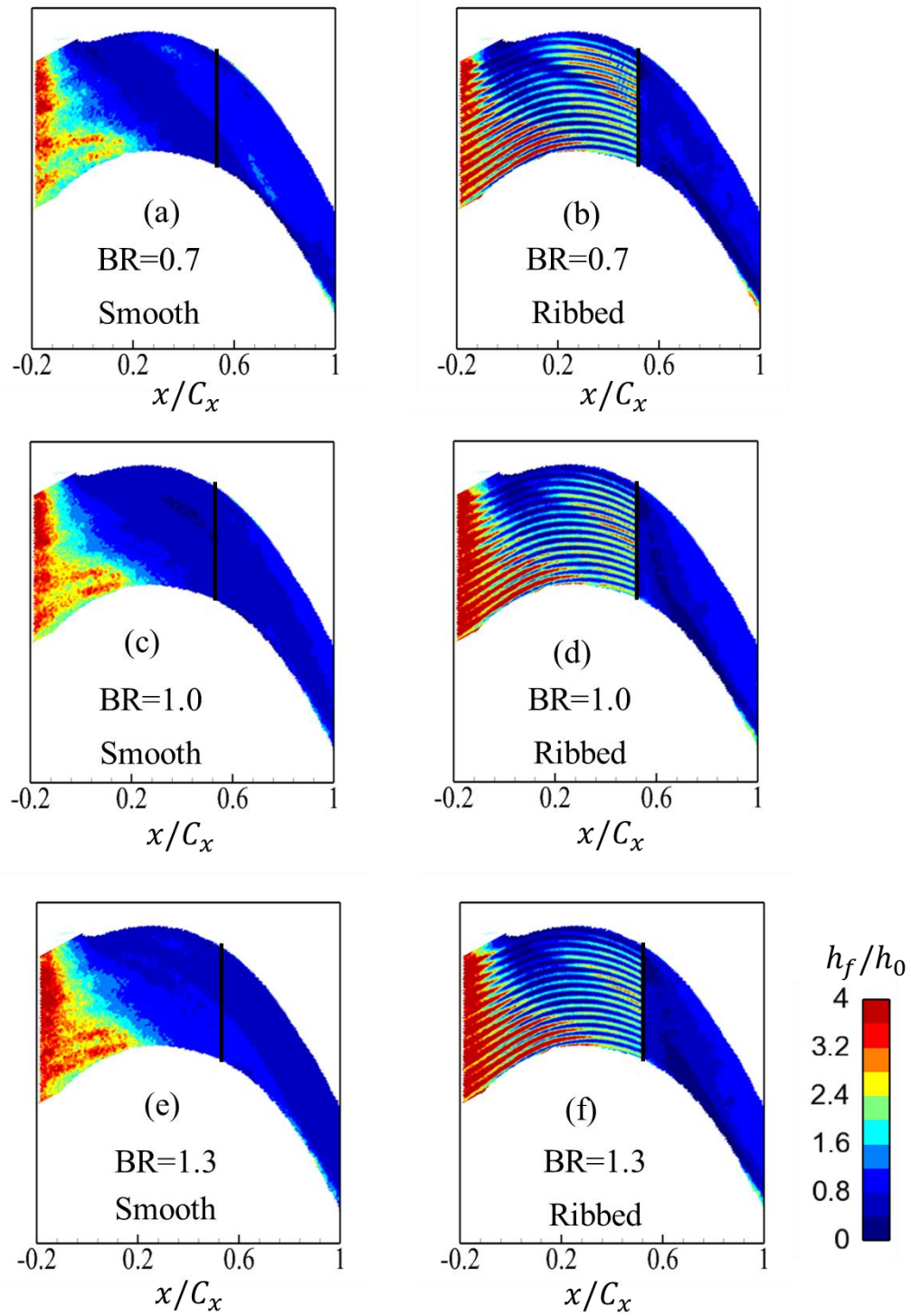


Figure 9. Distributions of h_f/h_0 . (experimental data)

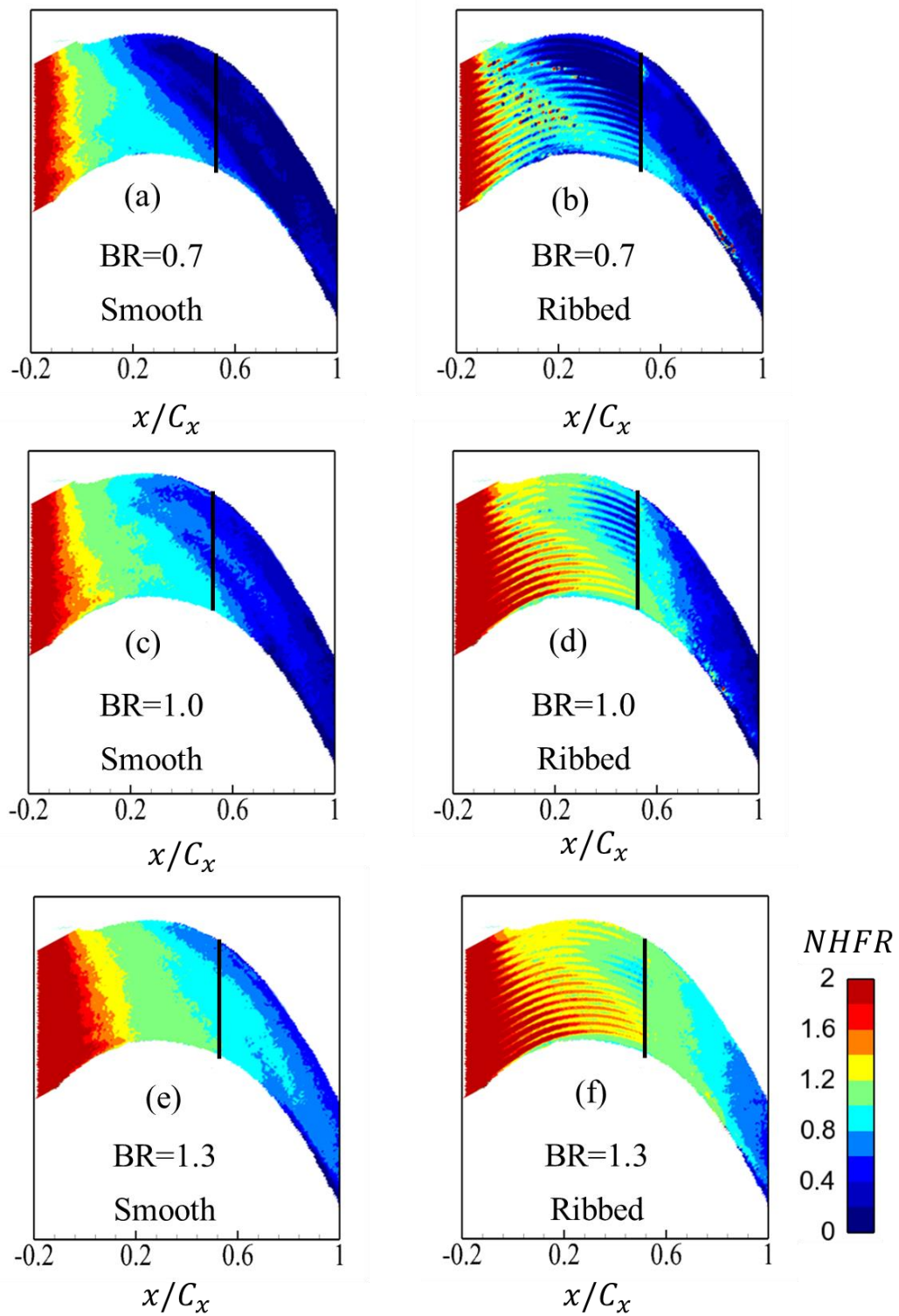
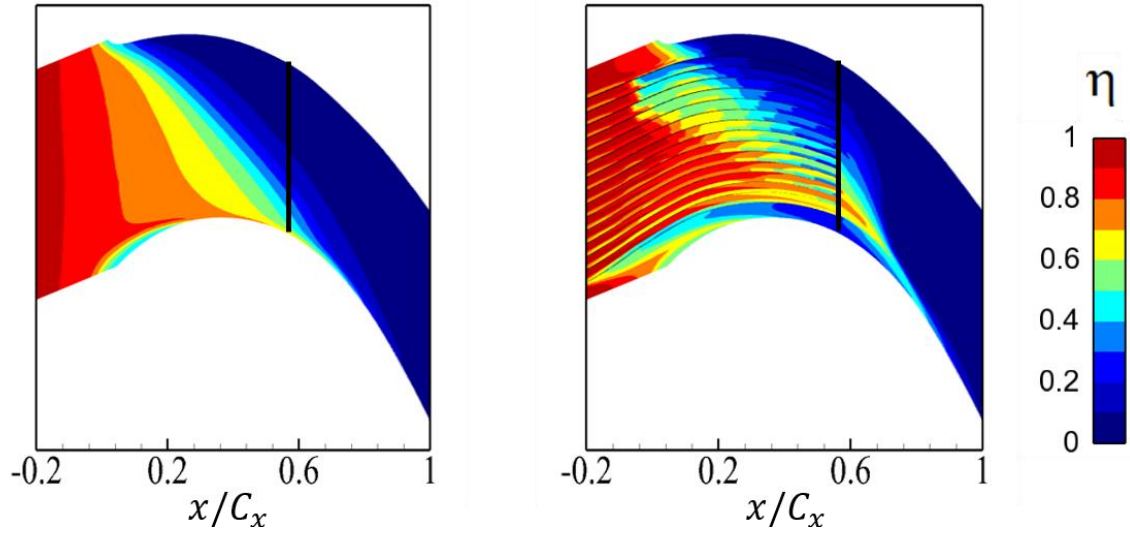


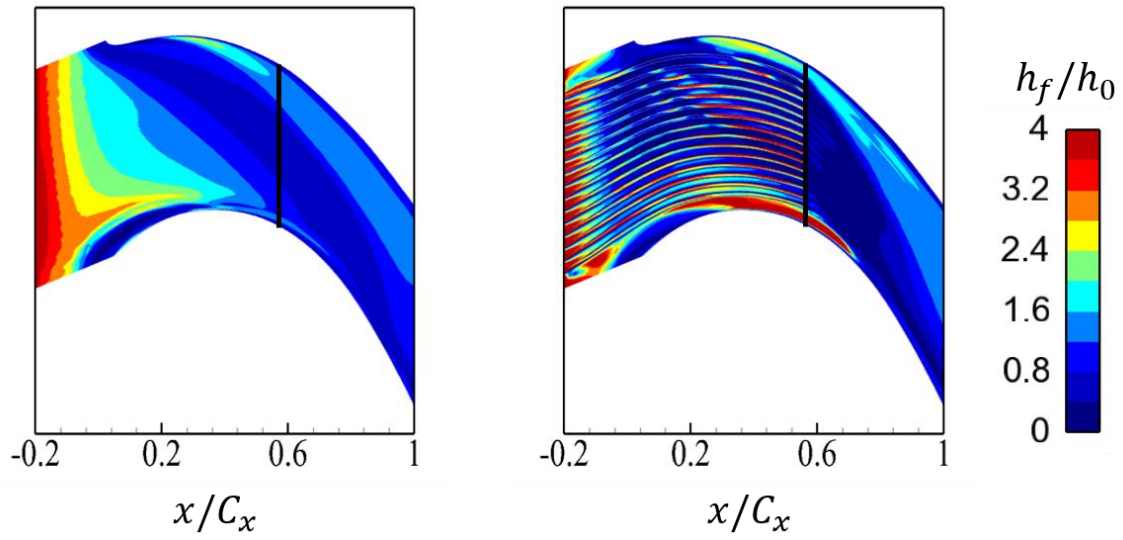
Figure 10. Distributions of NHFR. (experimental data)



(a) Smooth surface

(b) Ribbed surface

Figure 11. Distributions of film cooling effectiveness. (CFD results)



(a) Smooth surface

(b) Ribbed surface

Figure 12. Distribution of h_f/h_0 . (CFD results)

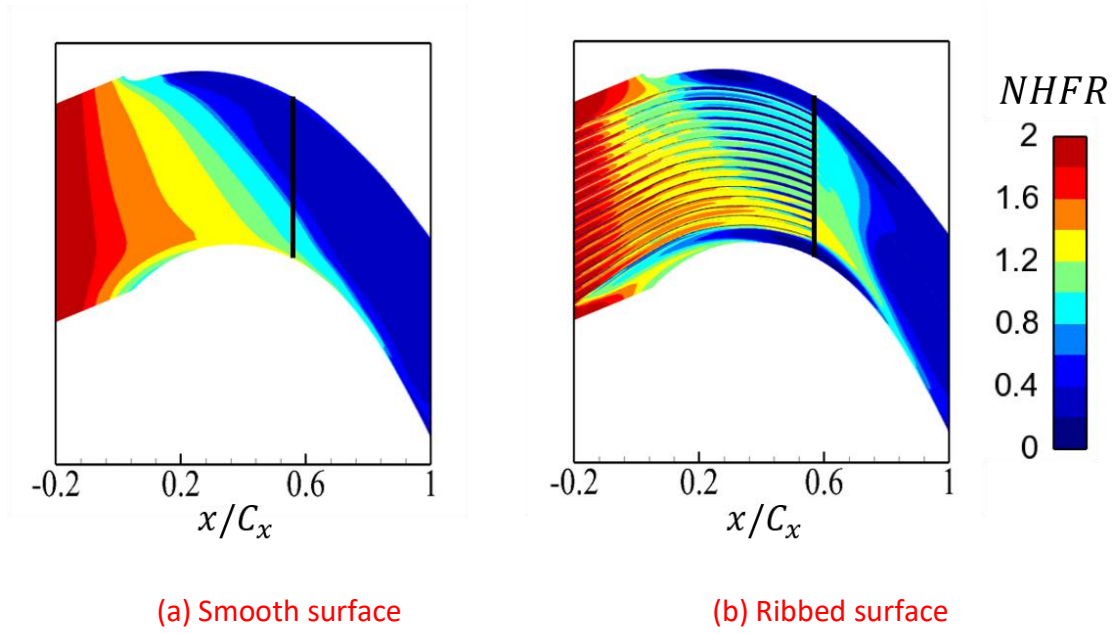
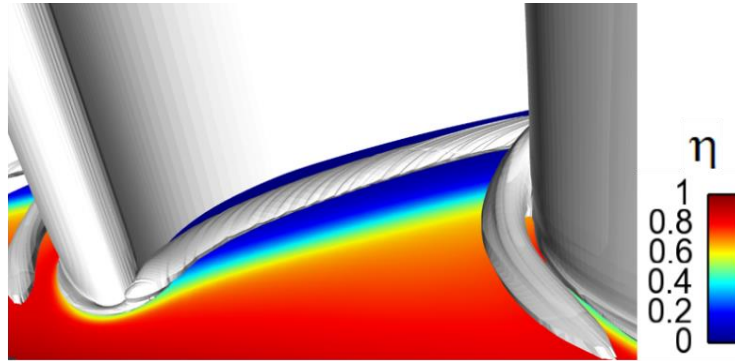
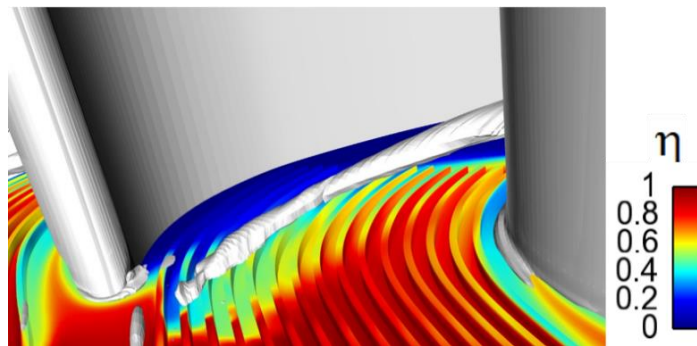


Figure 13. Distribution of NHFR. (CFD results)

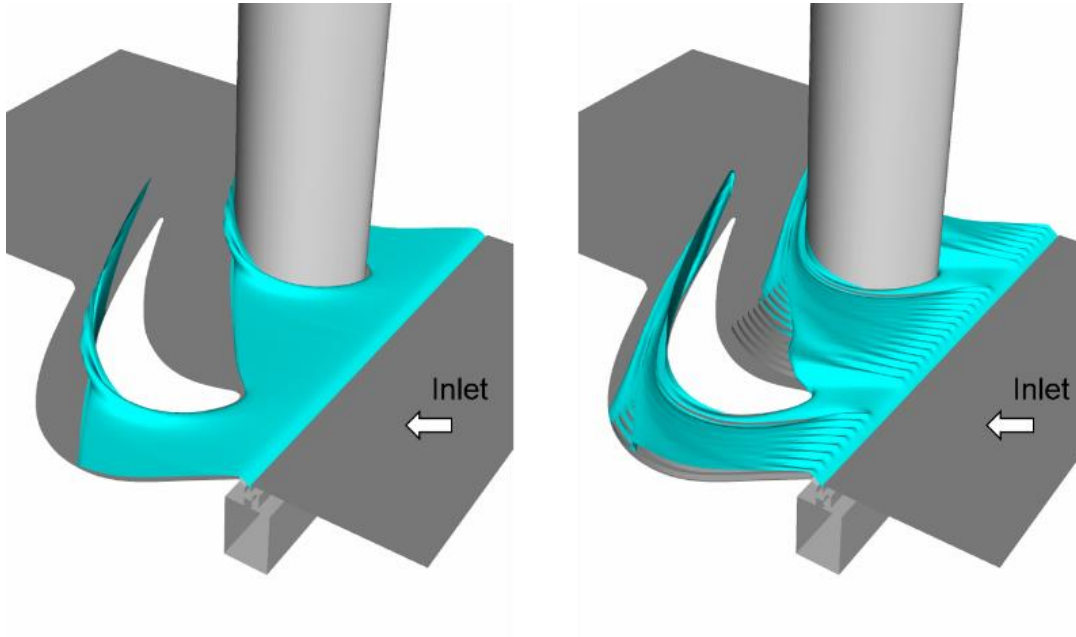


(a) Smooth surface



(b) Ribbed surface

Figure 14. Iso-surfaces of Q-criteria for smooth and ribbed surface.



(a) Smooth surface

(b) Ribbed surface

Figure 15. An iso-temperature surface with $\theta = 0.6$

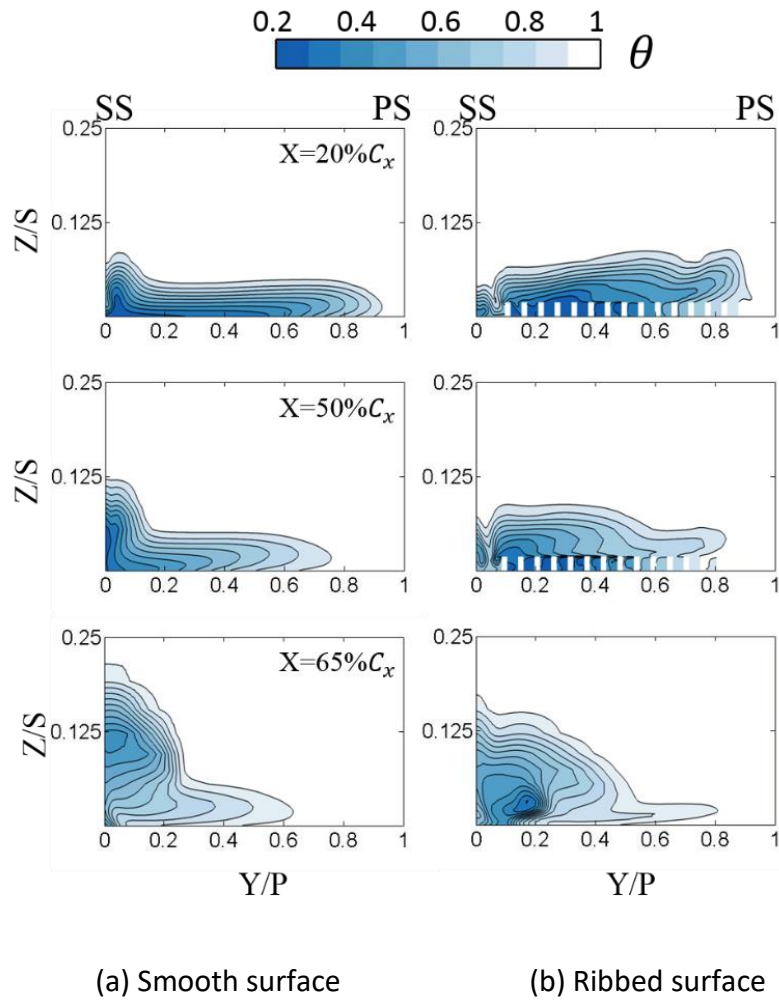


Figure 16. Non-dimensional temperature θ distributions at three cross sections.

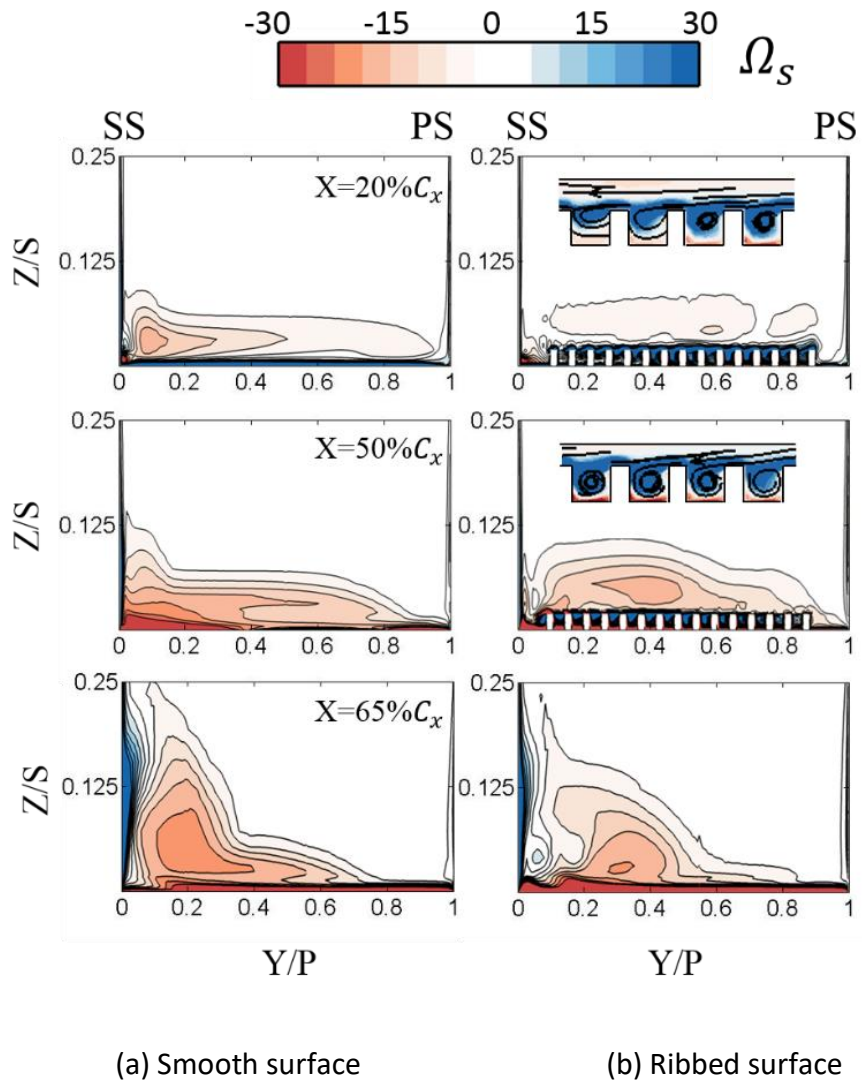
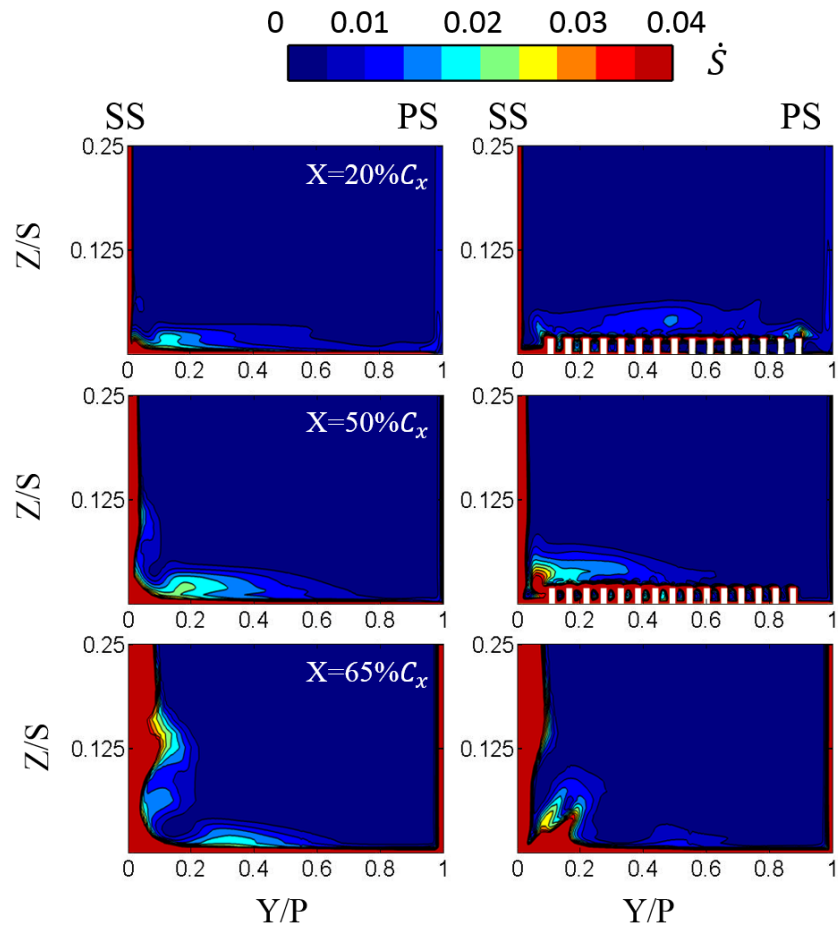


Figure 17. Streamwise vorticity distribution at three cross sections.



(a) Smooth surface (b) Ribbed surface

Figure 18: Dimensionless entropy generation rate per unit volume distributions at three cross sections.

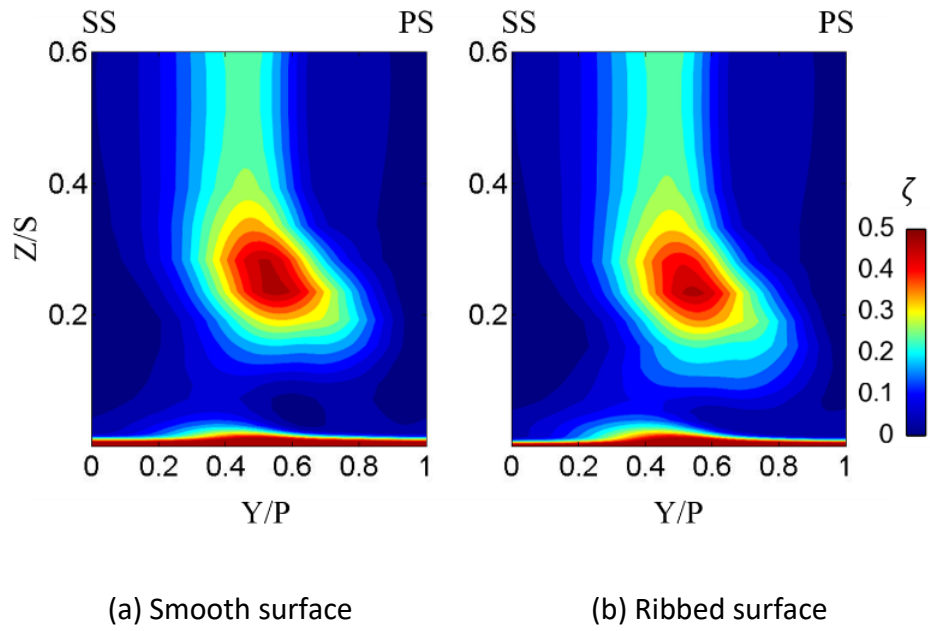
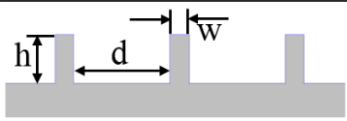


Figure 19. Distributions of Aerodynamic loss coefficient at the exit plane.

Table 1. Flow condition of the test section and blade geometries.

Inlet Reynolds number (based on C_x)	7.44×10^4
Exit Reynolds number (based on C_x)	1.86×10^5
Inlet boundary layer thickness	6mm
Inlet boundary layer momentum thickness	0.6mm
Purge air Blowing Ratio	0.7, 1.0, 1.3
Inlet flow angle (from axial)	35°
Mean exit flow angle (from axial)	72.49°
Axial chord	56mm
Pitch	56mm
Span	80mm
Inlet flow angle (from axial)	35°
Mean exit flow angle (from axial)	72.49°

Table 2. Geometry of ribs array on the end-wall.



h/P	0.026
w/P	0.017
d/P	0.089
δ/h	4

Table 3. Measurement uncertainties

Measurement	Relative uncertainty 95% confidence
Material property	5% ($564 \pm 28 \sqrt{s/m^2K}$)
Measured wall temperature	1K
h	9.7%
T_{ad}	0.3%